Nanoscale

Accepted Manuscript

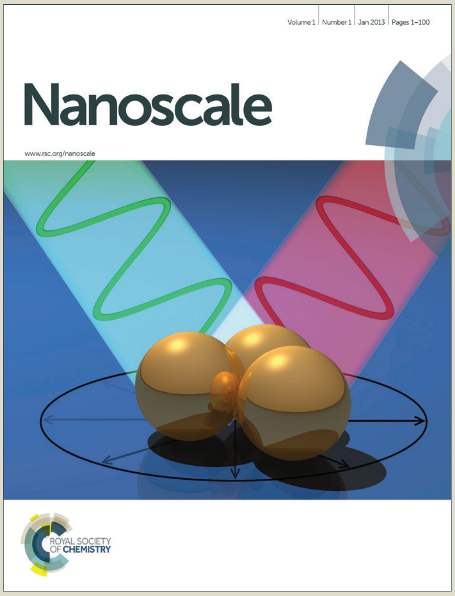

ROYAL SOCIETY OF CHEMISTRY

www.rsc.org/nanoscale

Journal Name RSCPublishing

ARTICLE

Cite this: DOI: 10.1039/x0xx00000x

Received 00th January 2012,
Accepted 00th January 2012

DOI: 10.1039/x0xx00000x

www.rsc.org/

Compliments of Confinements: Substitution and Dimension Induced Magnetic Origin and Band-Bending Mediated Photocatalytic Enhancements in $Bi_{1-x}Dy_xFeO_3$ Particulate and Fiber Nanostructures

M. Sakar,[a] S. Balakumar,[a,]* P. Saravanan,[b] and S. Bharathkumar[a]

The manifestation of substitution and dimensionalities induced modifications in magnetic origin and photocatalytic properties of Dy substituted bismuth ferrite (BDFOx) particulate and fiber nanostructures are reported herein. A gradual transformation from rhombohedral to orthorhombic structure is observed in BFO with increasing concentration of Dy. Substitution induced size reduction in particulate and fiber nanostructures is evident from the scanning and transmission electron micrographs. Energy band structure of both particulate and fiber nanostructures is considerably influenced by the Dy substitution that ascribed to the formation of new energy states underneath the conduction band of host BFO. Field dependent and temperature dependent magnetic studies reveal that the origin of magnetism in pure BFO system is due to the antiferromagnetic-core/ferromagnetic-shell like structure. On the other hand, it gets completely switched into 'canted' spin structures due to the substitution induced suppression of cycloidal spins in BFO, which is found to be the origin of magnetism in BDFOx particulate and fiber nanostructures. The visible light driven photocatalytic activity of BDFOx nanostructures is found to be enhanced with increasing concentration of Dy. Substitution induced band gap modification, semiconductor band bending phenomenon mediated charge transfer and reduced recombination resistances are attributed to the observed photocatalytic enhancements in these nanostructures.

1. Introduction

It is not an exaggerated fact that the advent of nanoscale science revealed the dimension dependent properties of materials. Such size characteristics of materials originated due to their quantum confinement at nanoscale.[1] This leads to the manifestation of quantum phenomena, where they essentially emerge due to the controlled movement of electrons in the materials. Thereby, materials' electronic and associated properties can become manipulative to certain extent as they largely governed by the transportation of the electrons/holes in the material. This is known as the dimension dependent properties of materials and this can be clearly perceived while comparing the materials of similar kind with different dimensions such as 3D particulate and 1D fiber nanostructures.[2]

Materials that show multifunctional properties would be appealing for the exploration of such dimension dependent properties. This is because of the phenomena that emerge in effect of their dimensionalities would be phenomenal in terms of their electronic, optical, magnetic and other functional properties.[3] This is in turn also revealing the origin of those properties in that particular multifunctional material. Among such materials, multiferroics have grabbed significant attention due to their simultaneous existence of multiple ferroic orders such as magnetic, ferroelectric, ferroelastic, etc.[4] Bismuth ferrite ($BiFeO_3$/BFO) is a well known multiferroic material that has been widely explored for their co-existence of magnetic and ferroelectric properties.[5] BFO is also being considered as an iconic material for the fundamental understanding of multiferroics as it shows the multiferroic properties at room temperature. BFO typically exhibits anti-ferromagnetic (AFM) and ferroelectric properties with very high Neel (~ 643 K) and Curie (~ 1100 K) temperatures respectively.[6] Studies on BFO have revealed that the fundamental prerequisite for a material to exhibit the ferroelectric-magnetic property is to have an appropriate *d* shell configuration. In BFO, the filled *d* shell leads to ferroelectric properties, while the empty *d* shell leads to the magnetic properties.[7] Therefore, control over the *d* shell configurations through chemical substitutions could cause a reasonable enhancement in its multiferroic properties. In addition to this, BFO is found to exhibit weak ferromagnetic properties when the particle size is reduced down to nanoscale.[8] From these literature reports it is apparent that the ferroelectric and magnetic properties of BFO could be due to the 'A' site Bi ions and the 'B' site Fe ions respectively.[9] In addition to this, any imbalance in the stoichiometric ratio between Bi, Fe and O ions also influences its multiferroic properties besides the ambiguity in the conditions for a material to exhibit the simultaneous ferroelectric-magnetic properties.[10]

The investigation on the origin of magnetism in BFO could reveal interesting insights into their magnetic phenomena. BFO demonstrates enhanced magnetic properties through (i) the suppression of its cycloidal AFM spin structures and (ii) the formation of AFM/FM core/shell structures.[11] The magnetic property that occurs due to one of these origins would also influence other properties of BFO. On the other hand, BFO also exhibits visible light driven photocatalytic activities that currently being explored for applications such as water splitting for hydrogen production and degradation of organic pollutants.[12] It is recently found that the ferroelectric property of materials plays important role in photocatalytic process.[13] Apart from the requirement of optimal band gap energy, a photocatalyst also requires effective mechanism for the charge separation and transportation of carriers to the photocatalyst-dye interfaces for the effective redox activities. Ferroelectric properties endow such functionalities to the photocatalyst through surface polarization charges. It presumably creates electrical field with surrounding medium and enhances redox reactions as well as the adsorption of dye molecules on the surface of photocatalyst. Further, ferroelectrics create 'lanes' for the charge carriers to be transferred to the surface and it greatly reduces the recombination possibilities in photocatalyst.[14] It is noteworthy that the band bending process also occurs in the semiconductors,[15,16] but it largely and instantaneously occurs in the ferroelectrics because of the polarized charges on their surfaces.

Therefore, to enhance the magnetic and photocatalytic properties, BFO has been modified in their chemical formulations through substitutions,[17] composites[18] and also in physical structure through morphology,[19] size[20] and dimensionalities.[21] In the perspective of dimensionalities, the one-dimensional systems such as fiber nanostructures can be explored for such dimension dependent studies as they have large aspect (diameter-to-length) ratio compared to other 1D nanostructures. It could be observed that the fiber nanostructures are made up of nanoparticulates that are stacked into one dimensional direction. The inter-connection between the nanoparticulates leads to an interfacial effects which is expected to enhance the magnetic as well as the photocatalytic interactions in these 1D materials.[22] In this context, we report here a comparative study on the characteristics role of dimension and chemical substitution in BFO particulate and fiber nanostructures on their magnetic and sunlight driven photocatalytic properties on the ability of degrading the organic dye molecule methylene blue (MB). The rare earth element dysprosium (Dy) is chosen as a substituent as it could enhance the magnetic property by suppressing the cycloidal spin structure in the host BFO.[23] Further, its optical property and 4*f* shell electronic configuration is expected to enhance the visible light absorption and photocatalytic properties.[24] It is also believed that the comparative investigation between the particulate and fiber nanostructures of BFO would possibly reveal their dimension dependent properties of at nanoscale.

2. Experimental

The precursor materials, bismuth nitrate [$Bi(NO_3)_3\,6H_2O$] (Puratronic®, 99.999%), iron nitrate [$Fe(NO_3)_3\,9H_2O$] (Puratronic®, 99.999%), and dysprosium nitrate [$Dy(NO_3)_3\,5H_2O$] (REacton®, 99.99%) and the solvents used were procured from the commercial resource (Alfa Aesar). The synthesis processes were carried out under normal ambient conditions.

2.1. Synthesis of $Bi_{1-x}Dy_xFeO_3$ nanoparticulates

The typical sol-gel method is adapted to synthesize nanoparticulates (NP_S) of $Bi_{1-x}Dy_xFeO_3$, (where $x = 0.0, 0.05, 0.10, 0.15, 0.20$, and 0.25).**[17,18]** For the synthesis of pure BFO particulates, equivalent grams of 0.1 M nitrates of bismuth and iron precursors are dissolved in 30 ml of double distilled (DD) water by adding 2 ml of 70% nitric acid (HNO_3). Then, 0.1 M of citric acid ($C_6H_8O_7$) dissolved in DD water is dripped into the above solution to obtain a homogeneous sol. Finally, the sol is heated up to ~80 ^{0}C to obtain the gel which is then dried to powders. The same procedure is repeated by adjusting the amount of bismuth nitrate and adding appropriate amount of dysprosium nitrate as per the composition formula to obtain the $Bi_{1-x}Dy_xFeO_3$ particulates. Finally, all the synthesized as-prepared powders were annealed at 650 ^{0}C for 3 h to obtain the required phase of the material.

2.2. Fabrication of $Bi_{1-x}Dy_xFeO_3$ nanofibers

The nanofibers (NFs) of $Bi_{1-x}Dy_xFeO_3$ (where $x = 0, 0.05, 0.1$, and 0.15) are fabricated by electrospinning technique.**[21]** For the fabrication of pure BFO fibers, equivalent grams of 0.8 M bismuth nitrate and iron nitrate precursors are dissolved in 5 ml of glacial acetic acid ($C_2H_4O_2$) to obtain a homogenous sol. To this, 1 g of polyvinyl pyrrolidone (PVP - M.W. 13, 00, 000) dissolved in 5 ml of DD water is added and stirred for 6 h to get a homogenous precursor gel for the electrospinning process. Then this solution is loaded in a plastic syringe equipped with stainless steel needle and connected to a high voltage of 15 kV with the solution flow rate of 0.2 ml/h. An aluminium foil spread-fiber collector is kept at a distance of 12 cm from the needle to collect the fibers. The same procedure is repeated by adjusting the amount of bismuth nitrate and adding the appropriate amount of dysprosium nitrate as per the composition formula to obtain $Bi_{1-x}Dy_xFeO_3$ nanofibers.

Subsequently, all the as-electrospun B(Dy)FO/PVP fibers are collected and annealed at 550 ^{0}C for 2 h to obtain the required phase of the materials.

It is found to be difficult to fabricate the BDFO$_x$ fibers at higher substitution concentrations ($x \geq 0.2$), where the as-spun fiber formation is itself too meagre and sticky, despite controlling the variables such as solution viscosity and applied voltage systematically. The electrospinning solution is basically ionic and its interaction with applied electric field is the crucial for the formation of fibers. Therefore, the introduction of Dy beyond certain concentrations causes some inadequacy in the ionic state/charge of the solution as a whole and suppresses the fiber formation. This suggests that still further studies are required to optimize the fabrication of BDFO$_x$ nanofibers for higher substitution concentrations.

2.3. Photocatalytic experiment

The fabricated $Bi_{1-x}Dy_xFeO_3$ particulate and fiber nanostructures are investigated for their photocatalytic activity on the degradation of methylene blue (MB) dye under the direct irradiation of sunlight. In a typical experiment, a stock of 10 ppm dye solution is prepared. From the stock, 100 ml of solution (1 ppm) is taken and the photocatalyst is added such as that the concentration of photocatalyst is 5 ppm in the 1 ppm of dye solution. This photocatalyst-dye mixture is kept and stirred well in dark condition for an optimized time of 30 min to obtain the adsorption-desorption equilibrium. Finally, this mixture is kept under the direct sunlight irradiation and the degradation of MB in terms of its optical absorbance characteristics is recorded at periodical intervals by using UV-Visible absorption spectrometer. The intensity of sunlight is monitored for every 30 min using LT-Lutron LX-10/A digital Lux meter. The average sunlight intensity over the whole duration of each experiment is calculated and found to be $1.2 \times 10^5 \pm 100$ lux.

As the photocatalytic experiments are conducted under sunlight irradiation, in order to minimize/avoid uncertainties due to the variation of sunlight intensity as a function of time, 2 to 3 trial experiments are carried out to check the consistency of the data obtained on everyday basis. Finally, the ideal experiments are carried out in a single day, with pre-planned and scheduled time. All the experiments were conducted in a tropical climate and under similar conditions on sunny days of April – May in Chennai, India (geographical location 13.04 ° North and 80.17 ° East on the Southern-East coast of India, between 10:00 a.m. and 03:00 p.m. outside temperature, 29 ℃ to 31 ℃).

3. Results and discussions

3.1. Crystal structure analysis

The phase and crystal structure analysis of the synthesized of $Bi_{1-x}Dy_xFeO_3$ particulate (where x = 0.0, 0.05, 0.10, 0.15, 0.20, 0.25) and fiber (where x = 0.0, 0.05, 0.10, 0.15) nanostructures are carried out by powder X-ray diffraction technique. XRD patterns over the range 20^{0} to 80^{0} as well as their respective doublet peak (31^{0} to 33^{0}) are shown in Fig. 1(a)-(b) and Fig. 2(a)-(b) respectively. The diffraction peaks are found to be matched with the standard JCPDS card # 71-2494 that revealed the rhombohedral crystal structure ($R3c$ space group) of $BiFeO_3$ phase. It can be noted that no additional peaks corresponding to any secondary or impurity phases appear in the XRD patterns of BDFO$_x$ particulates and fiber systems except in $Bi_{0.85}Dy_{0.15}FeO_3$ fibers.

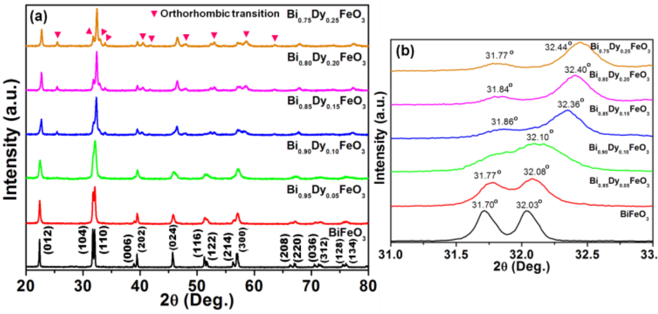

Fig. 1 (a) XRD pattern of $Bi_{1-x}Dy_xFeO_3$ particulates and **(b)** merging and shifting in doublet peaks

However, the following changes can be observed in the XRD patterns with increasing concentration of Dy in the host BFO nanostructures, (i) peak shifting, (ii) peak merging, and (iii) appearance of new peaks. Such observations reveal the occurrence of structural distortion and transformation in BFO due to the substitution of Dy ions. It should be noted that the appearance of new peaks at the 2θ positions, ~25.5^{0}, 27.8^{0}, 31.8^{0}, 32.9^{0}, 33.9^{0}, 40.5^{0}, 41.7^{0}, 53.1^{0}, 58.6^{0}, and 63.7^{0} in BDFO$_x$ ($x \geq 0.15$) could be due to the structural transitions in these compositions.[25]

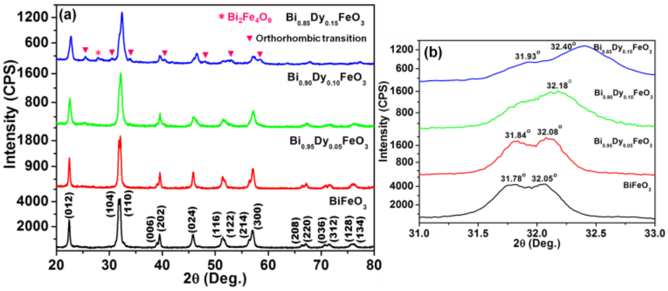

Fig. 2 (a) XRD pattern of $Bi_{1-x}Dy_xFeO_3$ fibers and **(b)** merging and shifting in doublet peaks

Khomchenko *et al*[25] have also observed similar XRD patterns of BDFO$_x$ for $x \geq 0.10$. It was explained from the results of their Rietveld refinement studies that the appearance of such new peaks essentially indicates the structural transformation of BFO from its parent rhombohedral to orthorhombic structure. Further, it is also reported that these XRD patterns are isostructural to their corresponding rare earth ferrites ($REFeO_3$), i.e., $DyFeO_3$ like phases, for $x \geq 0.15$.

Based on these observations, the following interpretations are proposed in the present work. The observed changes (peak merging and shifting) in the XRD pattern of BDFO$_x$ with increasing concentration of Dy may be reflecting the partial structural changes in BFO from its parent rhombohedral structure to orthorhombic structure. It can be noted in the XRD pattern of $Bi_{0.90}Dy_{0.10}FeO_3$ composition that the doublet peak is getting merged and likely coalesce into a single broad peak. On the other hand, appearance of new peaks and peak shift are also observed in the BDFO$_x$ compositions, for $x \geq 0.15$. It is also worth to note that the distance between the additional peak and main peak (indicated in Fig. 1(b) and Fig. 2(b)) is found to increase for concentrations above 15 % of Dy. This reflects the influence of ionic radii of the substituted ions over the structural transformations in the host BFO. It should be noted that the stable oxidation state of Dy ion is +3 and its ionic radius is 0.912 Å, which is smaller than the Bi^{3+} ions (1.03 Å).[26]

These observations suggest that the BDFO$_x$ compositions for $x \geq 0.15$ possess mixed phase of both rhombohedral ($R3c$) and orthorhombic phases.[25] To be specific, the orthorhombic structure of BDFO$_x$, for $x = 0.15$ may belong to *Pn*21*a* space group. Further increase of Dy ($x \geq 0.20$) may lead to *Pnma* space group where they likely become identical to $DyFeO_3$ phase as its parent structure is an orthorhombic *Pnma*. It is noteworthy that the *Pnma* is non-polar, while the *Pn*21*a* is polar that allows ionic displacement along the [010] direction. These results are in agreement with the other reports as well.[27,28]

The above observation is also consistent with BDFO$_x$ fiber compositions, where the increasing concentration of Dy in BFO fibers leads to the structural transition from the parent rhombohedral ($R3c$) to orthorhombic (*Pn*21*a*) structure. No peaks corresponding to the secondary/impurity phases are observed for BDFO$_x$ for Dy substitution up to 10 %. However, a peak with relatively very low intensity corresponding to $Bi_2Fe_4O_3$ phase starts appearing in $Bi_{0.85}Dy_{0.15}FeO_3$ composition and the new peaks at 2θ ~ 25.4^0, 31.9^0, 32.8^0, 40.5^0, 47.9^0, 53.0^0, 58.5^0 and 63.6^0 indicates the existence of orthorhombic phase along with the rhombohedral phase.

Table 1. Calculated crystallite size (t), micro-strain (ε), lattice parameters (a, c) and cell volume (V) of Bi1-xDyxFeO3 particulate and fiber compositions

Composition	T (nm)	ε	$a = b$ (Å)	c (Å)	V (Å^3)
			Particulates		
$BiFeO_3$	51	0.1306	5.579	13.872	431.77
$Bi_{0.95}Dy_{0.05}FeO_3$	39	0.2240	5.574	13.834	429.82
$Bi_{0.90}Dy_{0.10}FeO_3$	35	0.4582	5.576	13.671	425.06
$Bi_{0.85}Dy_{0.15}FeO_3$	32	0.2282	5.532	13.496	413.02
$Bi_{0.80}Dy_{0.20}FeO_3$	29	0.2160	5.519	13.5	411.20
$Bi_{0.75}Dy_{0.25}FeO_3$	41	0.2127	5.512	13.498	410.10
			Fibers		
$BiFeO_3$	27	0.3037	5.582	13.808	430.24
$Bi_{0.95}Dy_{0.05}FeO_3$	22	0.3660	5.586	13.675	426.71
$Bi_{0.90}Dy_{0.10}FeO_3$	18	0.4769	5.568	13.606	421.82
$Bi_{0.85}Dy_{0.15}FeO_3$	13	0.2595	5.534	13.633	417.51

t = crystallite size, ε = micro strain, a, b, c = lattice constants, V = cell volume

The average crystallite size of the synthesized pure BFO and BDFO$_x$ particulates and fibers are calculated by using the Scherrer's formula ($t = 0.9\ \lambda / \beta \cos\theta$), corresponding to (012), (104) and (110) planes. The lattice constants (a=b, c), cell volume (V), and the internal micro strain (ε) of these nanostructures are also calculated using the software supplied with the XRD instrument (X'pert High Score) and the values are tabulated in Table 1.

In general, for increasing concentration of Dy substitution, considerable reduction in the crystallite size of the BDFO$_x$ nanostructures is observed. This can be attributed to the substitution induced structural distortions in the system. The process of substitution-induced crystallite size reduction is possibly manifested as these substituted ions are likely play as impurities in the system that introduces anisotropicity and suppresses the growth of the individual crystallites. In the course of such formations, the characteristic properties of the substituted ions are important that include the ionic radius, oxidation state, electro-negativity of the substituents, etc.

3.2. Morphology analysis

The morphological analysis of the synthesized BDFO$_x$ particulate (where x = 0.0, 0.05, 0.10, 0.15, 0.20, 0.25) and fiber (where x = 0.0, 0.05, 0.10, 0.15) nanostructures are carried out by the field emission scanning electron microscopy (FESEM) and high resolution transmission electron microscopy (HRTEM) techniques. The obtained FESEM micrographs of particulates and fibers are shown in Fig. 3(a)-(f) and Fig. 4(a)-(d) respectively. Similarly, the obtained HRTEM micrographs of fibers are shown in Fig. 5(a)-(f) and Fig. 6(a)-(d) respectively.

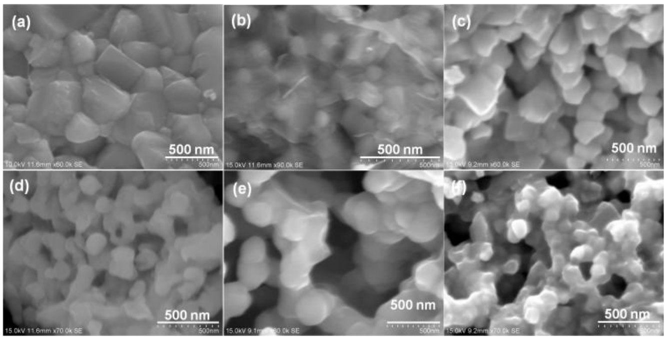

Fig. 3 FESEM micrograph of $Bi_{1-x}Dy_xFeO_3$ particulates for x = **(a)** 0.0, **(b)** 0.05, **(c)** 0.10, **(d)** 0.15, **(e)** 0.20, **(f)** 0.25, shows particle size decreasing with increasing concentration of Dy

The substitution of Dy is found to considerably influence the size of the particulates and fibers. The average size of the pure BFO particulates is found to be around 300 nm and the morphology is found to be a mixture of aggregated irregular/cubic morphologies. The overall size of the particulates gets reduced from 300 nm to 80 nm with substitution of Dy in the BFO host. The morphology is found to be modified to near spherical structure with increasing concentration of Dy and a noticeable control over the aggregation of particulates could also be observed.

It is known that the precursor solution of pure BFO contains only the nitrates of bismuth and iron along with citric acid (CA) and they effortlessly form as the product Bi-Fe-O. In such circumstances, the substitution of these ions in the solution acts as foreign elements (likely impurities) where the material formation has to occur along with these substituents (Dy^{3+}) and these ions should essentially make bonds with Fe, O as well as the neighbouring Bi ions in the lattice. This could largely influence the chemistry of particle formation as these ions have to be stabilized in the system and crystallized into the perovskite structure of BFO. Accordingly, they should strongly influence the other ions by making stronger bonds in order to accommodate these smaller ionic radii elements at the Bi site of the BFO host.

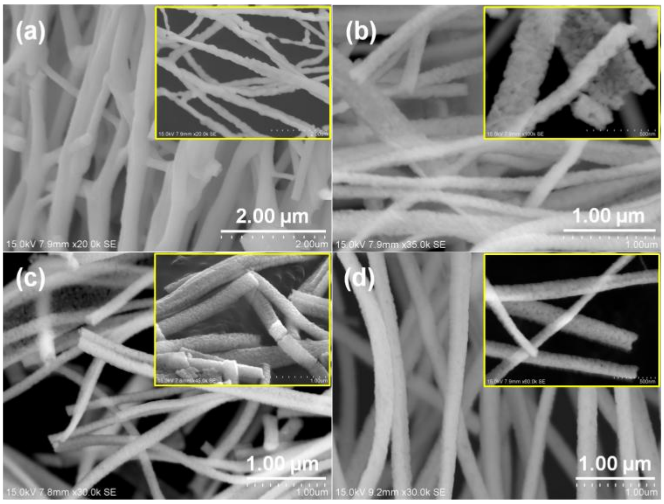

Fig. 4 FESEM micrograph of $Bi_{1-x}Dy_xFeO_3$ fibers where x = **(a)** 0.0, **(b)** 0.05, **(c)** 0.10, **(d)** 0.15. The insert images show the surface of the fibers

In such a process, the substitution of a smaller ionic radii element eventually leads to inhibit the particle growth and a reduction in the agglomeration as well as an influence in the particle morphology. Finally, the phase formation of these RE substituted BFO would be stabilized during the annealing process, and the particle size as well as morphology also evolved during the initial formation of the Bi-RE-Fe-O compositions.

Despite the role of ionic radius, the gelling agent-citric acid also plays an important role in determining the morphology of the particles. The gelling agent in the sol-gel process leads to the formation of stronger metal oxide structures which control the particle size as well as the morphology.[30] CA is acting as a surfactant, which controls the size and morphology of the particles through their binding habit on selective crystallographic facet of a growing crystal. Therefore, the interplay of CA owing to its selective binding habit[31] in the reaction leads to the transformation of irregular-cubic morphology to irregular-spherical morphology $BDFO_x$ particulates.

In the fiber nanostructures shown in Fig. 4(a)-(d), it could be observed that the fibers are made up of nano-granules that are stacked into one dimensional structure. Therefore, the size reduction in $BDFO_x$ fibers could be observed in terms of the size reduction of these nano-granules on the surface of fibers. It is evident that the Dy ions have an impact on controlling both the size as well as morphology of the host materials.

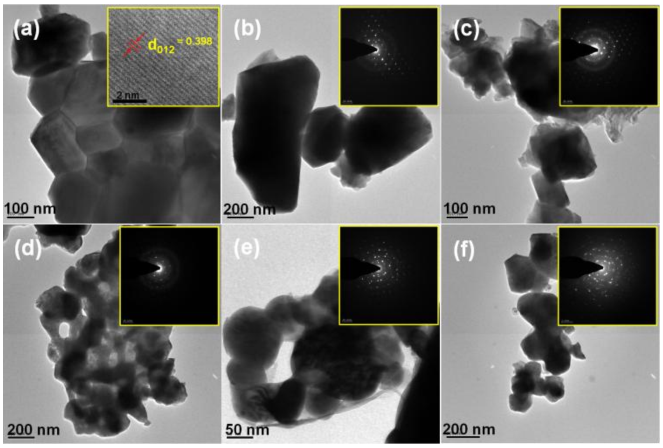

Fig. 5 HRTEM micrograph of $Bi_{1-x}Dy_xFeO_3$ particulates where x = **(a)** 0.0, **(b)** 0.05, **(c)** 0.10, **(d)** 0.15, **(e)** 0.20, **(f)** 0.25. Insert images show the **(a)** lattice fringes of pure BFO and **(b)-(f)** SAED pattern of the respective composition.

Accordingly, Dy substitution considerably reduced the size, and the aggregation among fibers is also found to be reduced. A closer view of the fiber (inset images of Figs. 4(a)-(d)) clearly shows that the nano-granules are densely packed without any gaps. The average diameter of $BDFO_x$ fibers is found to be 145 nm, 120 nm, and 100 nm, where x = 0.05, 0.10, 0.15, respectively.

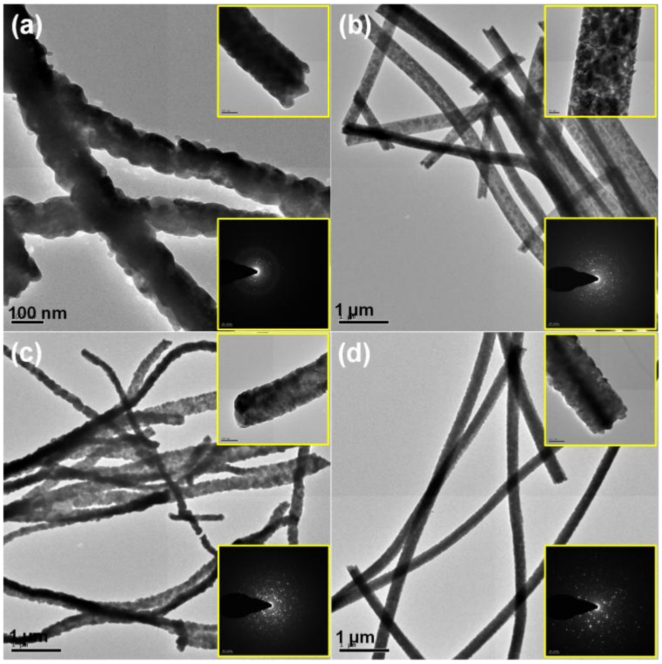

Fig. 6 HRTEM micrograph of $Bi_{1-x}Dy_xFeO_3$ fibers where x = **(a)** 0.0, **(b)** 0.05, **(c)** 0.10, **(d)** 0.15. Insert images show the closer view and SAED pattern of the respective fibers

The obtained HRTEM images are also in good agreement with the FESEM images. The observed lattice fringes of pure BFO particulates (insert of Fig. 5(a)) reveals that the BFO phase is formed with a high order of crystalline nature. From HRTEM image shown in Fig. 5(a), the rhombohedral structure of BFO is confirmed through the measured lattice distance of 0.398 nm along (012) plane. This value is consistent with the reported lattice distance value of rhombohedral-structured pure $BiFeO_3$ systems.[32-34] The selected area electron diffraction (SAED) pattern of $Bi_{1-x}Dy_xFeO_3$ particulate and fiber compositions (where $0 \leq x \leq 0.15$) (insert of Fig. 5(a)-(f) and Fig. 6(a)-(d)) show relatively a clear pattern revealing the enhanced crystalline phase of the compositions and more possibly a single phase system. Conversely, increasing concentration of substituents ≥ 0.20 leads to a complex SAED pattern. This may be due to the existence of mixed phases, which originated from the modification in the structure/phase transformation in these compositions.

In addition to this, the elemental analysis of these fabricated particulate and fiber nanostructures was also carried out by using the energy dispersive X-ray spectroscopy (EDS) technique and the obtained EDS spectra are shown Fig. S1(a)-(f) and Fig. S2(a)-(d), respectively in the Electronic Supplementary Information (ESI).

3.3. Estimation of band gap energy

The UV-Visible absorption spectra of $Bi_{1-x}Dy_xFeO_3$ particulate and fiber nanostructures are given in Fig. 7(a)-(b) respectively. The band gap energy of these nanostructures is deduced from their UV-Vis diffuse reflectance spectra (DRS) by applying Kubelka-Munk (KM) function.[35] The obtained DRS spectra of $Bi_{1-x}Dy_xFeO_3$ particulates (where x = 0.0, 0.05, 0.10, 0.15, 0.20, 0.25) and fiber (where x = 0.0, 0.05, 0.10, 0.15) nanostructures are shown Fig. S3(a)-(f) and Fig. S4(a)-(d) respectively in the ESI. The band gap energy of the materials is given in their respective DRS graph. It can be noted that in the case of particulates the band gap energy is considerably reduced from 2.35 eV to 2.26 eV with increasing concentration of Dy up to 20%.

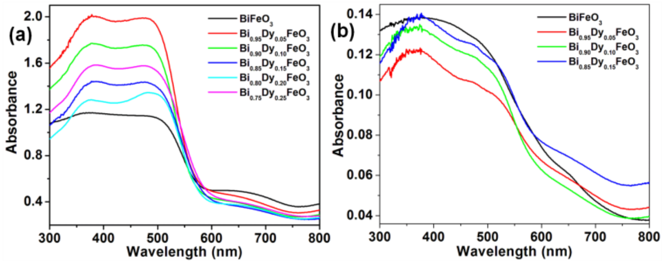

Fig. 7 UV-Vis absorption spectra of $Bi_{1-x}Dy_xFeO_3$ **(a)** particulate and **(b)** fiber nanostructures

In general, the substitution of rare earth (RE) ions show remarkable optical properties due to their electronic configuration ($4f^N$ $5s^2$ $5p^6$) both for divalent and trivalent ion.[36] The optical active electrons are in the 4f shell, so that they are not the outermost ones. They are shielded from external fields by two atomic shells with larger radial extension ($5s^2$ $5p^6$), which explains the atomic-like behaviour of their spectra.[36] Accordingly, the effective interactions between the RE ions and the electronic states of BFO can modify its optical properties very significantly. Therefore, the observed changes in the band gap energy could be attributed to the formation of new electronic states of Dy^{3+} ions underneath the conduction band (CB) of the host BFO. The hybridization between the Fe 3*d* and O 2*p* states essentially leads to the formation of optical band structures in BFO.[37] In particular, the top of the valence band is composed of strong hybridization among O 2*p*, Bi 6*p*, and Dy 4*f* states, and the bottom of the conduction band is led by Fe 3*d* states. Under such circumstances, the presence of Dy ions introduces 4*f* electron levels close to the lower edge of the CB and thus the photo-excited electrons in Dy substituted BFO can be transferred from O 2*p* to Dy 4*f* instead of Fe 3*d* states, considerably reducing the band gap energy as depicted in Fig. 8.

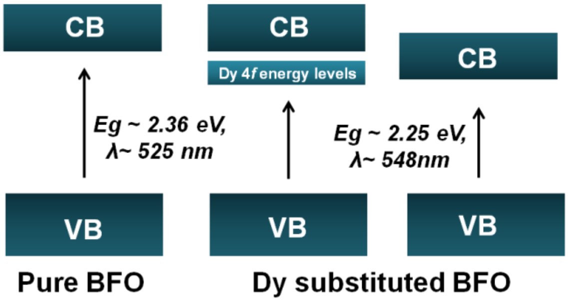

Fig. 8 Substitution induced reduction in the band gap energy of $Bi_{1-x}Dy_xFeO_3$ nanostructures

There is another perspective for the observed band gap reduction that could be attributed to the structural distortion-induced modification in this Dy substituted BFO nanostructures. The hybridization between Fe 3*d* and O 2*p* in turn depends on the Fe-O-Fe exchange angle and any change in the bond angle also alters the band gap of BFO.[38] The bond angle variation in Fe-O-Fe due to the Dy substitution could also be attributed to the reduced band gap energy in these compositions. It is evident from the XRD pattern that the 20 % and 25 % Dy substituted BFO reflect the $DyFeO_3$ phases. Hence the observed band gap increment in these compositions could have resulted from the structural transitions in these $BDFO_x$ nanostructures.

On the other hand, the band gap energy of pure BFO fibers is found to increase in comparison to pure particulates. Moreover, the increasing concentration of Dy substitution in BFO fibers also considerably increases the band gap energy. This could be due to the aspect ratio of the fibers, reduced crystallite size and the contribution of Dy ions in band structure formation in these 1D BFO. In fibers, it should be noted that there is only a small difference in the band gap energy with the increasing concentration of Dy ions. This indicates that the Dy ions tend to stabilize the perovskite structure of BFO fibers but do not lead to modify their band structures.

3. 4. Magnetization studies

The magnetic measurements of the synthesized particulate and fiber nanostructures are carried out using a super conducting quantum interference device (SQUID) magnetometer. The field dependent magnetic hysteresis (*M-H*) properties of the nanostructures are measured at room temperature (RT-300 K) as well as at low temperature (LT-5 K) at a maximum applied field of 2 T. Further, the temperature dependent (5 K to 300 K, at 100 Oe) zero-field cooling (M_{ZFC}) and field cooling (M_{FC}) magnetization studies are carried in order to investigate the origin of the magnetism in these nanostructures.

3.4.1. Magnetic hysteresis (*M-H*) properties

The RT and LT magnetic hysteresis (*M-H*) curves of $BDFO_x$, (where x = 0, 0.05, 0.10, 0.15, 0.20, 0.25) particulates are shown in Fig. 9(a)-(b) respectively. Similarly, Fig. 10(a)-(b) shows the RT and LT M-H curves of $BDFO_x$, (where x = 0, 0.05, 0.10, 0.15) fiber nanostructures.

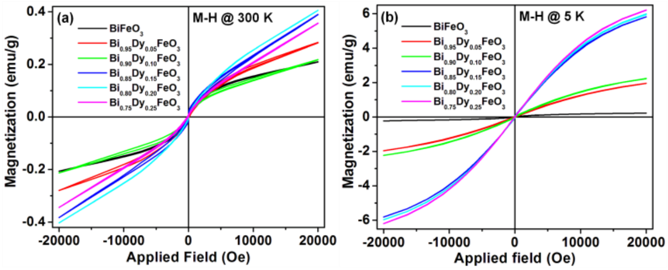

Fig. 9 M-H hysteresis curve of $Bi_{1-x}Dy_xFeO_3$ particulate nanostructures at **(a)** room temperature (300 K), and **(b)** low temperature (5 K)

In the case of particulates, a gradual enhancement in the magnetic hysteresis curves of $BDFO_x$ compositions can be observed with increasing concentration of Dy up to 20 % in RT measurements, while the gradual enhancement is observed up to 25% in LT measurements. In the case of fibers, the magnetic properties of $Bi_{0.95}Dy_{0.05}FeO_3$ and $Bi_{0.90}Dy_{0.10}FeO_3$ fibers are found to be decreased as compared to pure BFO fibers and a drastic enhancement can be observed in $Bi_{0.85}Dy_{0.15}FeO_3$ fibers. Alternatively, a gradual enhancement up to 15% could be observed in the LT M-H measurements. However, it should be noted that the overall magnetic saturation value of fibers (~ 1.0 emu/g) is found to be considerably enhanced compared to the particulates (~ 0.4 emu/g).

In general, the observed enhancements in both particulates and fibers BDFOx compositions could be due to the substitution induced suppression of the cycloidal spin structures in BFO, where the net magnetic moment is due to their uncompensated spins in the system.[39] This could be attributed to their reduced particle size, where it establishes a non-collinear spin arrangement in the system and thereby causing net magnetic moment in the material.[40]

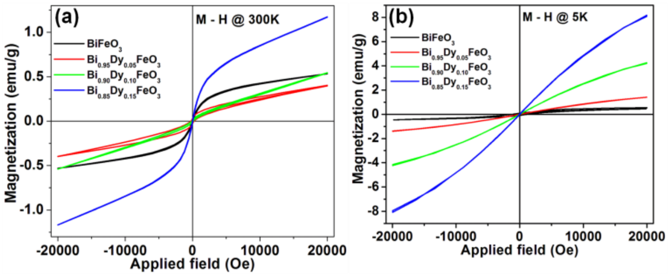

Fig. 10 M-H hysteresis curve of $Bi_{1-x}Dy_xFeO_3$ fiber nanostructures at **(a)** room temperature (300 K), and **(b)** low temperature (5 K)

In a broad context, the origin of enhancement in the magnetic properties of BFO could be either due to the formation of AFM/FM core/shell like structures or the suppression of its cycloidal spin structure that essentially leads to a net magnetization due to the manifestation of 'canted' spins.[41] Therefore, temperature dependent magnetization studies are carried out to probe the possible origin of the observed magnetism in these $BDFO_x$ nanostructures.

3.4.2. TEMPERATURE DEPENDENT MAGNETIZATION (M_{ZFC}, M_{FC}) PROPERTIES

Temperature dependent magnetization, i.e., ZFC and FC magnetizations (M_{ZFC}, M_{FC}) curves of $BDFO_x$ particulate and fiber compositions are shown in Fig. 11(a)-(f) and Fig. 12(a)-(d) respectively. It is evident that M_{ZFC}, M_{FC} curves are found to be completely different for $BDFO_x$ compositions in comparison to pure BFO. There are significant observations in the ZFC and FC curves of pure BFO particulates that essentially reflect the possible origin of the observed magnetism (Fig. 11(a)); (i) the splitting of ZFC and FC curves and (ii) a gradual increment and a drastic decrement of ZFC magnetic moments (M_{ZFC}) with decreasing temperature from 300 K to 5 K.

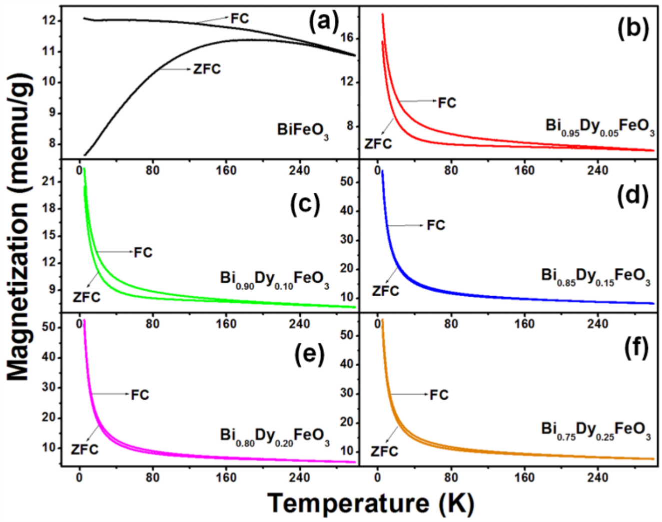

Fig.11 (a)-(f) Temperature dependent magnetization (M_{ZFC}-M_{FC}) curves of $Bi_{1-x}Dy_xFeO_3$ particulate nanostructures

Correspondingly, the observed splitting between ZFC and FC curves is essentially due to the coexistence of AFM and FM orderings in the system.[42] The initial increment in the M_{ZFC} with decreasing temperature and the plateau like region in the FC curve for lower temperatures indicate the existence of interacting superparamagnetic behaviour in pure BFO particulates.[43] It should be noted that superparamagnetism is the size effect of ferromagnetism. Therefore, the observed magnetic properties of pure BFO could be due to the mixed magnetic ordering of AFM-FM ordering. This may lead to the AFM/FM core/shell like structure in BFO.

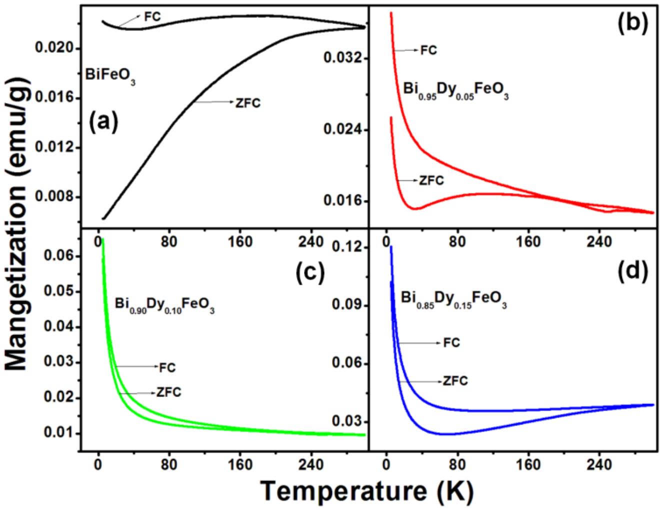

Fig. 14 (a)-(d) Temperature dependent magnetization (M_{ZFC}-M_{FC}) curves of $Bi_{1-x}Dy_xFeO_3$ fiber nanostructures

On the other hand, there is a variation observed in the M_{ZFC} curve of BFO fibers, where the ZFC magnetization is decreasing monotonically with decreasing temperature (Fig. 12(a)). In the case of particulate system, the ZFC magnetization shows a gradual increase up to a particular temperature, known as blocking temperature (T_B), and then starts decreasing with decreasing temperature. Further, the splitting/branching of M_{ZFC} curve occurs nearly at room temperature itself. This indicates that the T_B for fibers may possibly appear near room temperature. As already discussed, the T_B refers to the magnetic state of a material where its magnetic state would be ferro/super-paramagnetic before reaching T_B and it would turn into 'blocked state' after T_B.[44] This blocked state essentially means that the frozen state (reduced thermo-magnetic fluctuation) of magnetic moments where they do not respond to a smaller applied magnetic field and therefore the magnetic moments are decreasing with decreasing temperature. Accordingly, the persistence of blocked state at a lower temperature can also be corroborated with the observed weak ferromagnetic nature of the pure BFO fibers in *M-H* hysteresis measurements recorded at low temperature. In this context, it is more possible that the magnetic origin in pure BFO fibers could also be due to the AFM/FM core/shell like structures. However, the enhanced magnetization compared to particulates may be ascribed to the increased thickness of FM shell compared to the AFM core due to the one dimensional structuring of BFO.

In the case of $BDFO_x$ particulates, the observed small split in the M_{ZFC} curve of $Bi_{0.95}Dy_{0.05}FeO_3$ and $Bi_{0.90}Dy_{0.10}FeO_3$ compositions is due to the decreasing magnetization with decreasing temperature. On the other hand, a gradual enhancement in magnetization with decreasing temperature is observed for $0.15 \leq x \leq 0.25$. These observations essentially indicate the possible magnetic ordering in these compositions. Accordingly, it is apparent that the Dy substitution is found to enhance the canted spin structures by suppressing the cycloidal spin structures rather than leading to the formation of AFM/FM core/shell structures. Therefore, the branching of M_{ZFC} and M_{FC} in pure BFO essentially represents the existence of AFM/FM core/shell like structures, while the absence of such branching indicates the emergence of spin canted structure in Dy substituted BFO.

From the XRD patterns, a gradual structural transition can be observed in BFO with increasing Dy concentrations. Accordingly, this suppression of cycloidal spin structure can also be correlated to the observed structural transition from rhombohedral *R*3*c* structure to orthorhombic *Pnma* structure. It is already discussed that the substitution of RE ions at a higher concentration leads to the formation of a phase which is analogous to their corresponding $REFeO_3$ phase. Typically, the $REFeO_3$ phases possess an orthorhombic unit cell, which is existentially antiferromagnetic in nature.[45] Accordingly, the dominant AFM characteristics can be observed from the ZFC and FC magnetization curves, where the observed split gradually merges with increasing concentration of Dy in the BFO host. This essentially indicates that the Dy substitution facilitates the canted spin AFM ordering in BFO. Such system can be explained by Dzyaloshinskii-Moriya (DM) interactions.[46]

The fundamental idea of DM interaction is the induction of magnetization in antiferromagnets due to the modification in 'canted' spins as a result of the ferroelectric distortions.[47] Therefore, it can be suggested that the emerged magnetic ordering in $BDFO_x$ system is due to the modifications in its 'canted' spin structure (Fe-O-Fe) and it leads to the enhanced magnetic properties as illustrated in Fig. 13. It is noteworthy that the observed phenomenon is also known as 'ferroelectrically-induced ferromagnetism' which is generally due to this DM interaction in BFO.[48]

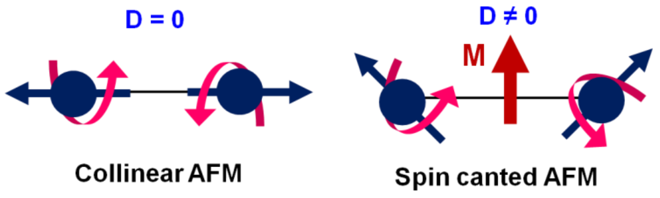

Fig. 13 Canted anti-ferromagnetic spin structures causing the net magnetic moments in Dy substituted BFO through Dzyaloshinskii-Moriya interactions

In addition to this, it should also be noted that the unit cell of Dy substituted perovskite structured BFO would consist of atoms which belong to different groups of transition elements Bi($4f^{14}$ $5d^{10}$ $6s^2$ $6p^3$), Dy($4f^{10}$ $6s^2$) and Fe($3d^6$ $4s^2$) with different magnetic moments. Therefore, the formation of magnetic ordering would have two components: (i) the antiferromagnetic contribution due to the canting of Fe sublattice and (ii) the contribution from the diamagnetism and paramagnetism of Bi and Dy ions respectively. When the temperature decreases, the number of canted spins is gradually increases and gets magnetized easily even at a lower applied magnetic field (in this study, it is 100 Oe). This may be due to the induced structural distortion in the system that affected the Fe-O-Fe interactions. Here, it is believed that the magnetic moments of the distorted FeO_6 octahedra are the main source of the magnetic properties due to the strong exchange interaction between the Fe sub-lattices. On the other hand, while increasing the temperature, the role of Bi and Dy ions become predominant and limits the magnetic property of the system as a whole. Therefore, the fundamental origin of the observed magnetic properties in Dy substituted BFO is due to the canted spin structures that emerges due to suppression of cycloidal spin structure. This can also be substantiated with the observed non-statured hysteresis curves.

It is evident that the M_{FC} and M_{ZFC} profiles of BDFO$_x$ fibers are also identical to the profiles observed for BDFO$_x$ particulates. Accordingly, the splitting of M_{ZFC} and M_{FC} curves is found to change with increasing concentration of Dy in BFO fibers which essentially indicates the modification occurring in the magnetic ordering in BFO. In $Bi_{0.95}Dy_{0.05}FeO_3$ fibers, M_{FC} value is monotonically increasing with decreasing temperature, while the ZFC measurements reveal a consistent increment in the magnetization for temperature below 50 K. For $Bi_{0.90}Dy_{0.10}FeO_3$ fibers a gradual increment in both M_{ZFC} and M_{FC} with decreasing temperature is observed. ZFC measurements on $Bi_{0.85}Dy_{0.15}FeO_3$ revealed a gradual decrement in magnetization up to 50 K and an increment below 50 K with decreasing temperature. In addition to this, the observed M_{ZFC} and M_{FC} curves of both BDFO$_x$ particulate and fiber nanostructures indicate their thermomagnetic reversibility characteristics, which could have originated due to their 'canted' spin structures.

The observed increment in magnetization at lower temperature indicates the interacting magnetic moments where they respond even at a low applied field (100 Oe). It should be noted that the very basis of the canted spin structure is AFM and therefore these canted spin structures always tend to respond at low temperature, thereby showing an increase in the magnetizations while decreasing the temperature. This observation can also be confirmed from the low temperature (5 K) *M-H* hysteresis curves of BDFO$_x$ fibers, where they exhibit the typical AFM characteristics (non-saturated magnetizations). Therefore, it is largely possible that the substitution of Dy ions enhances the magnetic ordering in BFO by inducing the canted spin structures, rather than leading to the AFM/FM core/shell like structure.

In the perspective of particulates *versus* fibers, the magnetic property of fibers is found to get enhanced compared to particulates. This could be attributed to their 1D structure, where it facilitates the magnetic alignments towards the *easy axis* of magnetization.[49] Due to the high aspect ratio of fibers, the spin canted structure along the unfettered dimension is found to be more pronounced compared to the fettered dimension. Such collective spin structures in fibers may induce the magnetic anisotropy where the magnetic spins respond largely to the applied magnetic field. In addition to this, it could be observed from the FESEM images that the fibers are made up of densely packed granules that gets stacked into 1D structure, where their inter-granule interactions would be very high and their surface properties are largely influential to any external stimuli. Thus, it is presumed that the emergence of canted spins is principally occurring on the surface, thereby these 1D structures largely receptive to the external magnetic field and magnetize effortlessly.

The observed values of the magnetic parameters such as saturation magnetization (M_s), remanent magnetization (M_r), and coercive field (H_c) of BDFO$_x$ particulate and fiber are given in Table 2.

Table 2. Room temperature (300 K) and low temperature (5 K) magnetization parameters of $Bi_{1-x}Dy_xFeO_3$ particulate and fiber nanostructures

Composition	**M_s (emu/g) @ 2T**		M_r (emu/g)		H_c (Oe)	
	300 K	5K	300 K	5 K	300 K	5 K
			Particulates			
$BiFeO_3$	0.21	0.23	0.002	0.012	32	199
$Bi_{0.95}Dy_{0.05}FeO_3$	0.28	1.96	0.009	0.022	177	154
$Bi_{0.90}Dy_{0.10}FeO_3$	0.23	2.24	0.006	0.018	22	28
$Bi_{0.85}Dy_{0.15}FeO_3$	0.39	5.82	0.005	0.053	18	29
$Bi_{0.80}Dy_{0.20}FeO_3$	0.42	5.98	0.004	0.037	24	31
$Bi_{0.75}Dy_{0.25}FeO_3$	0.36	6.22	0.008	0.021	199	41
			Fibers			
$BiFeO_3$	0.53	0.55	0.011	0.091	48	1239
$Bi_{0.95}Dy_{0.05}FeO_3$	0.40	1.42	0.029	0.004	265	42
$Bi_{0.90}Dy_{0.10}FeO_3$	0.55	4.27	0.012	0.013	119	43
$Bi_{0.85}Dy_{0.15}FeO_3$	1.17	8.18	0.013	0.025	25	44

3.5. Photocatalytic studies

The photocatalytic degradation spectra of methylene blue dye by BDFO$_x$, particulates (where x = 0.0, 0.05, 0.10, 0.15, 0.20, 0.25) and fibers (where x = 0.0, 0.05, 0.10, 0.15) are shown in Fig. S5(a)-(f) and Fig. S6(a)-(d) respectively in the ESI. Figure 14(a)-(b) shows the degradation efficiency C/C0 ratio graph and final degradation percentage of BDFO$_x$ particulates respectively. Similarly, Fig. 15(a)-(b) shows the degradation efficiency C/C_0 ratio graph and final degradation percentage of BDFO$_x$ fibers respectively. The overall efficiency of fiber nanostructures is found to get enhanced compared to particulates, where the fibers took 3 h to degrade the given amount of dye while the particulates took 4 h. It can be observed in BDFO$_x$ particulate compositions that the degradation efficiency is found to increase up to 15 %, and further increment of Dy to 20 % and 25 % leads to a decrement in the degradation efficiencies. In the case of fibers, both the 10% and 15% Dy substituted BFO fibers showed almost similar degradation percentages. Further, the photocatalytic efficiency of the fabricated nanostructures is also compared to the standard commercial TiO_2-P25 under similar experimental conditions and shown in Fig. 14(a) and Fig. 15(a).

In general, the observed trend in the photocatalytic efficiencies could be attributed to (i) the band gap energy of the compositions, and (ii) band bending phenomena that essentially inhibit the recombination possibilities and facilitate the transfer of charges to the photocatalyst-dye interfaces. It is known that the band gap energy determines the light absorption range of a photocatalyst and a narrow band gap energy profile endows a wide range of light absorption by the photocatalyst. The observed band gap reduction with increasing concentration of Dy could be attributed to the formation of new electronic states of 4*f* energy levels underneath the CB of BFO.[50] In such circumstances, owing to the half-filled electronic configuration, it can promote the charge transfer and efficiently separate the electron-hole pairs by trapping the electrons that limits the recombination possibilities in the Dy substituted BFO compared to pure BFO.

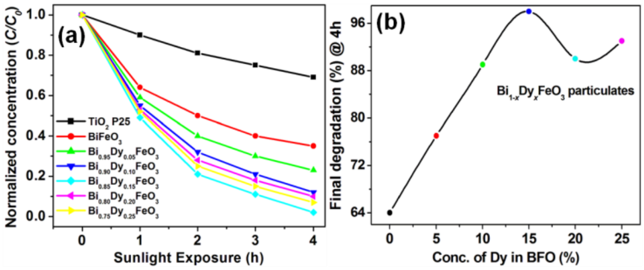

Fig. 14 Photocatalytic efficiency graphs of $Bi_{1-x}Dy_xFeO_3$ particulates, (a) Normalized concentration C/C_0-ratio and (b) Final degradation percentage of the individual composition

It is well known that half-filled electronic configuration is more stable. When Dy^{3+} ions trap electrons, the half-filled electronic configuration ($4f^{10}$) is destroyed and their stability decreases. The trapped electrons can thus be easily transferred to the oxygen molecules adsorbed on the surface of the catalysts, and the Dy^{3+} ions return to the original stable half-filled electronic structure. This might promote charge transfer and efficiently separate the electrons and holes by shallowly trapping electrons. The prerequisite for an effective substituent may involve the possibility of charge de-trapping and migration to the surface of catalysts. Thus, Dy substituted BFO has efficiency in the separation and transfer of charge carriers to the dye medium and shows improved degradation efficiency. This is a general possible mechanistic role of Dy^{3+} ions with half-filled *f*–shells that enhancing the photocatalytic activity.

In the case of $BDFO_x$ particulates, the photocatalytic efficiency is found to get decreased, when the concentration of RE ions is increased above 20 %. This may be due to the maximum optimal concentration of Dy (probably like a 'heavily doped semiconductor') that leads to the stabilization of the perovskite structure of BFO during the phase transitions rather than favouring the photocatalytic process. This may further lead to the screening of photocatalytic effect by means of increasing charge recombination effect in these particular compositions as evidenced in other systems.[51] Such possibilities could also be attributed to their increased band gap energy. The excess Dy ions at higher concentrations become the recombination centres for electron-hole pairs, and stabilize the charge separation efficiency of photo-generated carriers thereby inhibiting the enhancement of photocatalytic efficiencies.

In another perspective, the role of band bending on the photocatalytic process is very interesting as it facilitates the migration of charge carriers to the dye-photocatalyst interface thereby enhancing the degradation of the dye through the production of active redox species. This band-bending model can be demonstrated in semiconductors in terms of their *conducting type* (*n*/*p*-type) and in ferroelectrics in terms of their ferroelectric polarizations.[13,14,16] However, this band-bending phenomenon is under considerable debate and their formations and mechanisms are yet to be explored for a better understanding. Moreover, it is more complex in the BFO system as it is a 'ferroelectric-semiconductor' and this band-bending phenomenon exists in both semiconductors and ferroelectric materials.

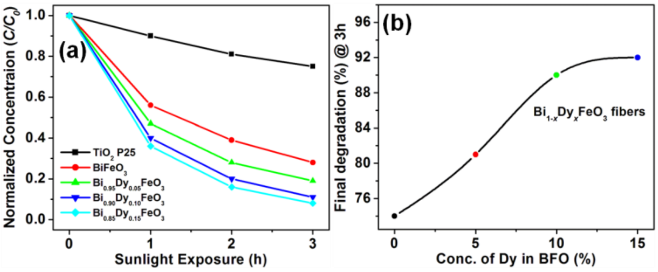

Fig. 15 Photocatalytic efficiency graphs of $Bi_{1-x}Dy_xFeO_3$ fibers, (a) Normalized concentration C/C_0-ratio and (b) Final degradation percentage of the individual composition

Based on these factors, we propose the band-bending model and associated photocatalytic process in BFO as follows. As mentioned, the bands of semiconductor materials tend to bend depending upon the *conducting type* of the semiconductor.[52,53] On the other hand, the bands of ferroelectric materials tend to bend depending upon the direction of the polarization in the material as shown in Fig. 16(a)-(d).[13, 14, 54, 55] In this case, when the BFO is exposed to light, the electron-hole pairs will be induced and the electrons would migrate towards the surface, while the holes would move away from the surface and the vice versa when the polarization direction switches. The electrons excited to the surface would be further transferred to the BFO-dye interface and facilitate the degradation of dye molecules through the reduction process. While, the holes would directly react with the dye molecules and possibly degrade the dye molecules as given in the eqn. (1)-(4).[56]

Absorption of efficient photons by photocatalyst (PC)

$$PC + h\nu \rightarrow e^-_{cb} + h^+_{vb} \tag{1}$$

formation of superoxide radical anion

$$O_2 + e^-_{cb} \rightarrow O_2^{\bullet -} \tag{2}$$

Oxidation of the organic pollutants (R) via successive attack by ${}^{\bullet}OH$ radicals

$$R + {}^{\bullet}OH \rightarrow R'^{\bullet} + H_2O \quad (3)$$

or by direct reaction with holes

$$R + h^{+}_{vb} \rightarrow R^{\bullet} + \rightarrow \text{degradation products} \quad (4)$$

It is generally observed that increasing the concentration of Dy in the BFO host leads to structural distortion in the system. Hence, it may increase the polarizability of the domains which causes the effective band bending and enhances the photocatalytic activity. It should be clearly noted that this band bending process also inhibits the charge recombination in BFO as the electrons are more likely driven to the surface and holes are driven away from the surface.

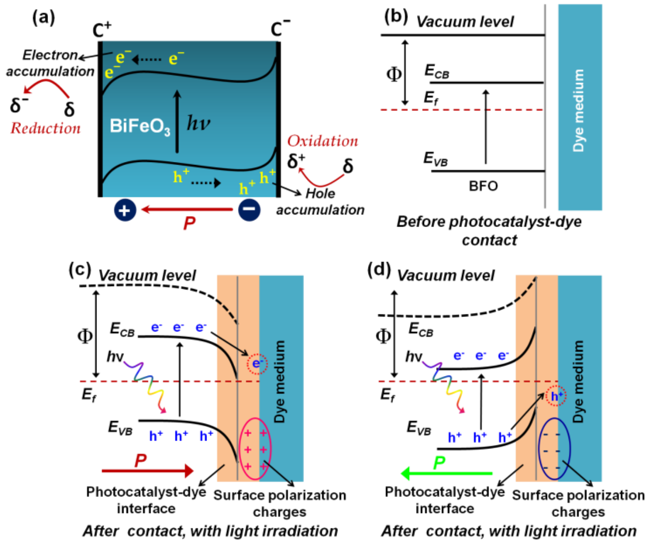

Fig. 16(a) Depiction of the band bending phenomenon occurring in ferroelectric-semiconductor photocatalyst (FSP), (b) before the contact of FSP with dye medium and (c)-(d) emergence of polarization direction dependent band bending after the contact of FSP-dye along with the light irradiation

In this context, in our study, the observed photocatalytic activity of the BDFO$_x$ compositions could be attributed to this band-bending process associated with its enhanced electrical domains with increasing concentration of Dy possibly up to 15 %. It is known that the off-centre ionic displacement in the unit cells causes the structural distortion in the system. Accordingly, it can be observed from the XRD analysis that the space group of BFO is *R*3*c* which is polar that allows the ionic displacement in the system. Further, it is expected that the substitution of Dy in BFO host would increase this structural distortion and enhance the polarizability of these compositions. This can be corroborated with the XRD results that for increasing concentration of Dy up to 15 % led to the structural changes from rhombohedral to orthorhombic structure with the mixed space group of *R*3*c* as well as *Pn*21*a* which is also a polar and allows the polar displacements in the BFO system. However, further increment of Dy, i.e., 20 % and 25 % led to the formation of $DyFeO_3$ like phase with space group *Pnma*. This is a non-polar space group and may lead to limit the ionic displacement via stabilizing the perovskite structure, in such a way that the crystal structure becomes complex and it may affect the band bending process due to the suppression of ionic displacements in these compositions. The observed relative decrement in the photocatalytic efficiency could be attributed to decrement in the polarizability of these compositions for higher substitution concentrations. Hence, it is possible that a ferroelectric to paraelectric transition might have taken place when the concentration of Dy is increased above 20 % thereby decreasing the photocatalytic efficiency.

On the other hand, in the case of fibers, the observed trend in the photocatalytic efficiencies could be attributed to its one-dimensional structure along with other factors such as band gap energy, and band bending phenomena that inhibit the recombination possibilities. Here, the elongated structure decreases the recombination possibilities of photo-generated carriers due to an increased delocalization of electrons.[57] Further, it can be observed that the surface of the fibers appears like inter-connected crystallite structure where it is possible for the excited carriers generated in these inter-connected crystallites to reach the surface whereby they also actively involved in the photocatalytic process through enhanced interactions with the dye molecules.

The observed efficiency in these one-dimensional fibers could be directly ascribed to the synergic effect resulting from their confined and unconfined dimensions. The unfettered dimension of these 1D materials essentially decreases the recombination probabilities of photo-generated charge carries (e^-/h^+) due to the enhanced recombination resistance,[58] while the fettered direction influences the charge transferring mechanisms due to the formation of discrete energy levels as a result of the confinement in these inter-connected nano-granules. In 1D materials, once the charge-separation is established in the system, the electrons get excited and get localized in the conduction band (CB) of the host. Eventually, it delays the recombination possibilities of charge carriers in these 1D materials. Under such circumstances, the energy applied for charge separation is sustained in the system and utilized for the production of redox species in the medium that leads to the effective degradation of the dye molecules.

4. Conclusion

$Bi_{1-x}Dy_xFeO_3$ particulate (where $x = 0.0, 0.05, 0.1, 0.15, 0.2, 0.25$) and fiber ($x = 0.0, 0.05, 0.1, 0.15$) nanostructures are synthesized by sol-gel and electrospinning methods respectively. Dy substitution is found to influence the crystal structure which gets changed from rhombohedral to orthorhombic structure. The new peaks appeared in the XRD pattern of BDFO$_x$ particulates for $x = 0.20, 0.25$ indicates the isostructural characteristics of $DyFeO_3$ phase. The FESEM and HRTEM micrographs depict the irregular morphology of the particulates and the fibers that are found to be a stacking of nano-granules into 1D structure. The size, shape and agglomeration of these nanostructures are gradually modified with increasing concentration of Dy in the BFO host, that attributed to the smaller ionic radius of Dy ions compared to Bi ions. The optical properties of these nanostructures investigated from the UV-Visible diffuse reflectance spectra showed that band gap energy of the BFO is found decreasing with concentration of Dy. The observed band gap tunability is attributed to the substitution induced formation of new energy states underneath the conduction band of the host BFO. The observed relative increment in band gap energy of BFO fibers could be attributed to their nanostructured granules in the 1D structure. The magnetic properties investigation by SQUID magnetometer revealed the characteristic origin of magnetism in these pure and Dy substituted nanostructures. The field dependent (*M-H*) hysteresis curves obtained at low temperature and room temperature showed a gradual enhancement in the magnetic properties of these nanostructures. Origin of magnetism in these nanostructures is probed via performing the temperature dependent (ZFC and FC) magnetization studies. Accordingly, the observed branching phenomenon in ZFC-FC curves indicated that the fundamental origin of magnetism in pure BFO nanostructures to be core/shell like structuring of antiferromagnetic/ferromagnetic spins respectively. While, the observed thermo-magnetic reversibility and net magnetic moments indicated that the origin of magnetism in $BDFO_x$ nanostructures is the 'canted' spin structures that emerge due to the substitution induced suppression of cycloidal spin structure. Further, the observed relative enhancements in the magnetic properties of fibers could be due to their 1D structuring, which led to the rhombohedral distortions in the FeO_6 octahedron along [111] direction and the formation of magnetic domains that largely consisting the spins with *easy axis* of magnetizations. The photocatalytic efficiency is found to get enhanced with increasing concentration of Dy in BFO host. It is attributed to the reduced band gap energy and ferroelectric property mediated charge transfer process through band bending phenomena in these compositions. Further, the reduced recombination resistance and enhanced delocalization of charge carriers are attributed to the enhanced photocatalytic activity of fiber nanostructures.

Acknowledgements

The authors gratefully acknowledge the Council of Scientific and Industrial Research (80(0074)/10/EMR-II, dt. 30-12-2010), and one of the authors M. Sakar acknowledges the NCNSNT-MHRD grants for the postdoctoral research fellowship (C-2/NSNT/pdf/2014/044, dt. 24-01-2014), to carry out this research project.

Notes and references

[a] National Centre for Nanoscience and Nanotechnology, University of Madras, Guindy Campus, Chennai 600 0025, India. Fax: 044-22352494/22353309; Tel: 044-22202749; *E-mail: balasuga@yahoo.com
[b] Defence Metallurgical Research Laboratory, Hyderabad 500 058, India.

Electronic Supplementary Information (ESI) available

1. (a) R. Emil, *Chem. Soc. Rev.*, 2006, **35**, 583; (b) L. Aballe, A. Barinov, A. Locatelli, S. Heun, M. Kiskinova, *Phys. Rev. Lett.*, 2004, **93**, 196103.
2. M. Bannwarth, D. Crespy, *Chem. Asian J.*, 2014, **9**, 2030.
3. (a) P. R. Sajanlal, T. S. Sreeprasad, A. Samal, T. Pradeep, *Nano Reviews*, 2011, **2**, 5883; (b) R. K. Joshi, J. J. Schneider, *Chem. Soc. Rev.*, 2012, **41**, 5285.
4. (a) N. A. Spaldin, M. Fiebig, *Science*, 2005, **309**, 391; (b) S. W. Cheong, M. Mostovoy, *Nat. Mate.*, 2007, **6**, 13.
5. G. Catalan, J. F. Scott, *Adv. Mater.* 2009, **21**, 2463.
6. C. Ederer, N. A. Spaldin, *Phys. Rev. B* 2005, **71**, 060401.
7. N. A. Hill, *J. Phys. Chem. B*, 2000, **104**, 6694.
8. R. Mazumder, P. Sujatha Devi, D. Bhattacharya, P. Choudhury, A. Sen, M. Raja, *Appl. Phys. Lett.*, 2007, **91**, 062510.
9. C. H. Yang, D. Kan, I. Takeuchi, V. Nagarajan, J. Seidel, *Phys. Chem. Chem. Phys.*, 2012, **14**, 15953.
10. C. Ederer, N. A. Spaldin, *Phys. Rev. B*, 2005, **71**, 224103.
11. (a) M. Sakar, S. Balakumar, P. Saravanan, S. N. Jaisankar, *Mater. Res. Bull.*, 2013, **48**, 2878; (b) K. Chakrabarti, B. Sarkar, V. D. Ashok, K. Das, S. S. Chaudhuri, S. K. De, *Nanotechnology*, 2013, **24**, 505711.
12. (a) F. Gao, X. Chen, K. Yin, S. Dong, Z. Ren, F. Yuan, T. Yu, Z. Zou, J. M. Liu, *Adv. Mater.*, 2007, **19**, 2889; (b) W. Ji, K. Yao, Y. F. Lim, Y. C. Liang, A. Suwardi, *Appl. Phys. Lett.*, 2013, **103**, 062901.
13. Y. Cui, J. Briscoe**,** S. Dunn, *Chem. Mater.*, 2013, **25**, 4215.
14. L. Li, P. A. Salvador, G. S. Rohrer, *Nanoscale*, 2014, **6**, 24.
15. A. L. Linsebigler, G. Lu, J. T. Jr. Yates, *Chem. Rev.*, 1995, **95**, 735.
16. Z. Zhang, J. T, Jr. Yates, *Chem. Rev.*, 2012, **112**, 5520.
17. (a) M. Sakar, S. Balakumar, I. Bhaumik, P. K. Gupta, S. N. Jaisankar, *RSC Adv.*, 2014, **4**, 16871; (b) R. Guo, L. Fang, W. Dong, F. Zheng, M. Shen, *J. Phys. Chem. C*, 2010, 114, 21390.
18. (a) M. Sakar, S. Balakumar, P. Saravanan, S. N. Jaisankar, *AIP Conf. Proc.*, 2013, 1512, 228; (b) S. Li, Y. H. Lin, B. P. Zhang, J. F. Li, C. W. Nan, *J. Appl. Phys.*, 2009, 105, 054310.
19. S. Li, Y. H. Lin, B. P. Zhang, J. F. Li, C. W. Nan, *J. Phys. Chem. C*, 2010, **114**, 2903.
20. T. Xian, H. Yang, J. F. Dai, Z. Q. Wei, J. Y. Ma, W. J. Feng, *Mate. Lett.*, 2011, **65**, 1573.
21. (a) M. Sakar, S. Balakumar, *RSC Adv.*, 2013, 3, 23737.; (b) S. H. Xie, J. Y. Li, Roger Proksch, Y. M. Liu, Y. C. Zhou, Y. Y. Liu, Y. Ou, L. N. Lan, Y. Qiao, *Appl. Phys. Lett.*, 2008, 93, 222904; (c) A. Baji, Y. W. Mai, Q. Li, S. C. Wong, Y. Liu, Q. W. Yao, *Nanotechnology*, 2011, 22, 235702
22. B. Weng, S. Liu, Z. R. Tang, Y. J. Xu, *RSC Adv.*, 2014, **4**, 12685.
23. P. Uniyal, K. L. Yadav, *J. Phys.: Condens. Matter*, 2009, **21**, 012205.
24. A. Khataee, R. D. C. Soltani, Y. Hanifehpour, M. Safarpour, H. G. Ranjbar, S. W. Joo, *Ind. Eng. Chem. Res*., 2014, **53**, 1924.
25. V. A. Khomchenko, D. V. Karpinsky, A. L. Kholkin, N. A. Sobolev, G. N. Kakazei, J. P. Araujo, I. O. Troyanchuk, B. F. O. Costa, J. A. Paixao, *J. Appl. Phys.* 2010, **108**, 074109.
26. R. S. Shannon, *Acta Crystallogr.*, 1976, **A32**, 751.
27. Y. Li, J. Yu, J. Li, C. Zheng, Y. Wu, Y. Zhao, M. Wang, Y. Wang, *J Mater Sci: Mater Electron.* 2011, **22**, 323.
28. V. A. Khomchenko, J. A. Paixao, D. A. Kiselev, A. L. Kholkin, *Mater. Res. Bull.*, 2010, **45**, 416.
29. Z. Shuxia, W. Lei, C.Yao, W. Dongliang, Y. Yingbang, M. Yanwei, *J. Appl. Phys.*, 2012, **111**, 074105.
30. H. Yuning, J. Yi, Z. Ya, *J. Mole. Catal. A: Chem.*, 2010, **331**, 15.
31. X. Yujie, *Chem. Commun.* 2011, **47**, 1580.
32. T. J. Park, G. C. Papaefthymiou, A. J. Viescas, A. R. Moodenbaugh, S. S. Wong, *Nano Lett.*, 2007, **7**, 766.
33. Y. G. Wang, G. Xu, Z. H. Ren, X. Wei, W. J. Weng, P. Du, G. Shen, G. R. Han, *J. Am. Ceram. Soc.*, 2007, **90**, 2615.

34. S. H. Xie, J. Y. Li, R. Proksch, Y. M. Liu, Y. C. Zhou, Y. Y. Liu, Y. Ou, L. N. Lan, Y. Qiao, *Appl. Phys. Lett.*, 2008, **93**, 222904.
35. S. V. M. Pavana, C. Karthik, R. Ubic, M. S. Ramachandra Rao, C. Sudakar, *Appl. Phys. Lett.*, 2013, **103**, 022910.
36. P. C. Sati, M. Arora, S. Chauhan, M. Kumar, S. Chhoker, *J. Phy. Chem. of Solids*, 2014, **75**, 105.
37. W. Hai, Z. Yue, M. Q. Cai, H. Haitao, L. W. C. Helen, *Solid State Commun.*, 2009, **149**, 641.
38. Z. Zhang, P. Wu, L. Chen, J. Wang, *J. Appl. Phys.*, 2010, **96**, 012905.
39. M. Muneeswaran, N. V. Giridharan, *J. Appl. Phys.* 2014, **115**, 214109.
40. R. C. Lennox, M. C. Price, W. Jamieson, M. Jura, A. D. Aladine, C. A. Murray, C. Tang, D. C. Arnold, *J. Mater. Chem. C*, 2014, **2**, 3345.
41. J. Bertinshaw, D. L. Cortie, Z. X. Cheng, M. Avdeev, A. J. Studer, F. Klose, C. Ulrich, X. L. Wang, *Phys. Rev. B*, 2014, **89**, 144422.
42. H. Fengzhen, W. Zhijun, L. Xiaomei, Z. Junting, M. Kangli, L. Weiwei, T. Ruixia, X. TingTing, H. Ju, Y. Chen, Z. Jinsong, *Sci. Rep.* 2013, **3**, 2907.
43. D. P. Dutta, P. M. Balaji, N. Ratna, L. Gavin, A. K. Tyagi, *J. Phys. Chem. C*, 2013, **117**, 2382.
44. D. P. Dutta, G. Sharma, A. K. Rajarajan, S. M. Yusuf, G. K. Dey, *Chem. Mater.*, 2007, **19**, 1221.
45. L. A. Prelorendjo, C. E. Johnson, M. F. Thomas, B. M. Wanklyn, *J. Phys. C: Solid State Phys.*, 1980, **13**, 2567.
46. C. Ederer, C. J. Fennie, *J. Phys.: Condens. Matter*, 2008, **20**, 434219.
47. H. J. Feng, *J. Magn. Magn. Mater.*, 2010, **322**, 1765.
48. D. L. Fox, J. F. Scott, *J. Phys. C: Solid State Phys.*, 1977, **10**, L329.
49. R. E. Lu, K. G. Chang, B. Fu, Y. J. Shen, M. W. Xu, S. Yang, X. P. Song, M. Liu, Y. D. Yang, *J. Mater. Chem. C*, 2014, **2**, 8578.
50. (a) A. H. Krumpel, E. van der Kolk, D. Zeelenberg, A. J. J. Bos, K. W. Kramer, P. Dorenbos, *J. Appl. Phys.*, 2008, **104**, 073505; (b) A. J. Kenyon, *Prog. Quant. Electron.*, 2002, **26**, 225.
51. (a) W. Ping, S. Larissa, M. Roland, W. Michael, *J. Mater. Chem. A*, 2014, **2**, 8815; (b) H. Hongwei, L. Xiaowei, H. Xu, T. Na, Z. Yihe, Z. Tierui, *Phys. Chem. Chem. Phys.*, 2015, **17**, 3673.
52. X. Zhang, Y. L. Chen, R. S. Liu, D. P. Tsai, *Rep. Prog. Phys.*, 2013, 76, 046401.
53. (a) M. Sakar, S. Balakumar, S. Ganesamoorthy, *J. Mater. Chem. C*, 2014, 2, 6835; (b) Z. Zhen, W. Ping, C. Lang, W. Junling, *Appl. Phys. Lett.*, 2010, 96, 232906.
54. C. R. Bowen, H. A. Kim, P. M. Weaver, S. Dunn, *Energy Environ. Sci.*, 2014, 7, 25
55. Y. Zhang, A. M. Schultz, P. A. Salvador, G. S. Rohrer, *J. Mater. Chem.*, 2011, 21, 4168.
56. Malik Mohibbul Haque, Detlef Bahnemann, Mohammad Muneer, Photocatalytic Degradation of Organic Pollutants: Mechanisms and Kinetics, Organic Pollutants Ten Years After the Stockholm Convention - Environmental and Analytical Update, Dr. Tomasz Puzyn (Ed.), ISBN: 978-953-307-917-2, InTech, 2012, DOI: 10.5772/34522.
57. (a) A. Leelavathi, M. Giridhar, N. Ravishankar, *Phys. Chem. Chem. Phys.*, 2013, **15**, 10795; (b) E. Naveen Kumar, J. Rajan, P. A. Archana, C. Vijila, R. Seeram, *J. Phys. Chem. C*, 2012, **116**, 22112.
58. (a) M. Kunal, T. H. Teng, J. Rajan, R. Seeram, *Appl. Phys. Lett.*, 2009, **95**, 012101; (b) B. Matthias, *Energy Environ. Sci.*, 2011, **4**, 3275.